JGR Space Physics

RESEARCH ARTICLE
10.1029/2021JA029758

Characterizing Satellite Path Through Kelvin-Helmholtz Instability Using a Mixing Parameter

A. Settino[1,2], Yu V. Khotyaintsev[2], D. B. Graham[2], D. Perrone[3], and F. Valentini[1]

[1]Dipartimento di Fisica, Università della Calabria, Rende, Italy, [2]Swedish Institute of Space Physics, Uppsala, Sweden, [3]ASI–Italian Space Agency, Rome, Italy

Key Points:

- We introduce the mixing parameter for *in situ* measurements of Kelvin-Helmholtz instability
- We use the mixing parameter to identify the evolutionary phase of the Kelvin-Helmholtz instability and the magnetospheric multiscale crossings of vortices
- We observed more rolled-up vortices at a late time of the instability due to changes in the solar wind conditions

Correspondence to:
A. Settino,
adriana.settino@unical.it

Citation:
Settino, A., Khotyaintsev, Y. V., Graham, D. B., Perrone, D., & Valentini, F. (2022). Characterizing satellite path through Kelvin-Helmholtz instability using a mixing parameter. *Journal of Geophysical Research: Space Physics*, *127*, e2021JA029758. https://doi.org/10.1029/2021JA029758

Received 6 JUL 2021
Accepted 10 JAN 2022

Abstract We introduce the mixing parameter to analyze the *in situ* measurements of a Kelvin-Helmholtz event observed by the Magnetospheric Multiscale mission. We define the mixing parameter, for both ions and electrons, using the well distinct particle energies which characterize the magnetosphere and magnetosheath plasmas. This parameter nicely identifies the different populations which are interacting at the Earth's magnetopause and the boundaries of Kelvin-Helmholtz vortices. Thus, we analyze the crossing of each structure into a parameter space defined as the space of the electron mixing versus the ion mixing, where specific shapes occur according to the evolutionary phase of the Kelvin-Helmholtz instability. All along the event, we observe three different types of shapes, namely a straight line, a simple loop, and a complex loop, which likely corresponds to linear waves, steepened waves, and rolled-up vortices, respectively. The most complex shape (rolled-up vortex) is observed mostly at the end of the interval, owing to fast growth of the instability which is connected to variations of the solar wind magnetic field orientation.

Plain Language Summary The Kelvin-Helmholtz instability is a ubiquitous phenomenon in space plasmas, which can develop at velocity shears, such as the ones observed at the interaction regions between the fast and slow solar wind and at the Earth's magnetopause. In the latter case, plasmas with different properties, namely the low density magnetospheric and high-density magnetosheath plasmas, interact and mix. The evolutionary development of the instability is mainly characterized by three phases, which correspond to a different degree of mixing of both ions and electrons in the magnetosheath and magnetosphere. When the threshold condition is satisfied (which typically corresponds to a super Alfvénic velocity jump) the instability grows linearly and surface waves are generated. At later times, the pressure gradient comes into play, leading to the mixing of the two layers and the generation of vortices. As the instability develops, the mixing degree of the particles of each layer increases and more and more rolled-up vortices are observed. In this work, we use the mixing degree of ions and electrons to establish which phase the instability is undergoing and to identify the boundaries of the structures.

1. Introduction

The Kelvin-Helmholtz (KH) instability is a physical phenomenon that can develop in both fluids and plasmas in correspondence with velocity shears when a threshold condition is satisfied (Chandrasekhar, 1961; Drazin, 2002; Miura, 1982). In particular, magnetized plasmas are unstable when the jump flow is locally super Alfvénic, due to the stabilizing effect of the magnetic field. The KH instability, after initial exponential growth, generates a train of large-scale vortices that, through nonlinear interactions, can eventually evolve and merge. In the context of space plasmas, the KH instability has been observed in several environments, for example, at the interface of coronal mass ejections (Foullon et al., 2011), at planetary magnetopauses (Fairfield et al., 2000; Hasegawa et al., 2004, 2006; Kivelson & Chen, 1995), and recently in the slow solar wind (Kieokaew et al., 2021).

In situ measurements in the near-Earth plasma environment have revealed a permanent boundary layer where electromagnetic waves have been detected close to the polar cap and similar to those observed at the low latitude boundary layer (Lakhina & Tsurutani, 1999; Tsurutani et al., 1998, 2001). During periods of northward interplanetary magnetic field (IMF), the boundary layer is further thickened at low latitudes when KH instability is favored, but magnetic reconnection at the subsolar magnetopause tends to be suppressed (Fairfield et al., 2000; Hasegawa et al., 2004; Otto & Fairfield, 2000). Thus, in this configuration, the KH instability is thought to play a major role in the plasma entry. Indeed, it can lead to the local violation of the frozen-in condition with the generation of possible reconnection sites inside the vortices, which enhance the entry of plasma (Foullon et al., 2008;

Kavosi & Raeder, 2015; Nykyri et al., 2006; Nykyri & Otto, 2001). It is worth mentioning that besides magnetic reconnection, other input mechanisms of energy have been proposed, such as viscous-like interactions (Axford & Hines, 1961) that broadly include the KH process at the magnetopause (Chen & Hasegawa, 1974) and cross-field particle diffusion (Tsurutani & Thorne, 1982). Recently, the NASA magnetospheric multiscale (MMS) mission has provided new insights into the KH instability by allowing a deeper study of its interplay with magnetic reconnection (Eriksson et al., 2016; W. Li et al., 2016; Nakamura et al., 2017). In addition, the unprecedented high-resolution measurements provided by MMS enabled the study of the kinetic dynamics of the KH instability, pointing out the multi-scale nature of the phenomenon (Sorriso-Valvo et al., 2019; Stawarz et al., 2016), with a particular focus on the distortions of the ion distribution functions (Settino et al., 2021) in agreement with numerical experiments (Settino et al., 2020).

The evolution of the KH instability has also been analyzed from a numerical point of view using both fluid and kinetic approaches. In particular, kinetic approaches showed a different growth rate of the instability due to the relative sign between the vorticity and the magnetic field; thus highlighting the important role of the kinetic effects on the dynamics of the instability (Henri et al., 2012, 2013). Moreover, in configurations where the magnetic field changes sign across the shear layer, the KH instability is coupled to magnetic reconnection, which contributes to the transfer of momentum between the plasma on the two sides of the shear (Faganello & Califano, 2017). The interconnection between KH instability and magnetic reconnection has been studied also in a three-dimensional geometry either when KH instability is the primary process that drives magnetic reconnection and vice versa when magnetic reconnection starts first and triggers the KH instability (Ma et al., 2014a, 2014b). During the fully nonlinear phase, the KH instability can drive secondary instabilities like the Rayleigh-Taylor, secondary KH, or tearing instabilities, which can lead to the disruption of the vortices (Faganello et al., 2008; Matsumoto & Hoshino, 2004), thus affecting the plasma transport.

Both simulations and *in situ* measurements showed the important role played by the KH instability on the complex dynamics of the Earth's magnetopause, contributing either to the local plasma heating or to the enhancement of the boundary layer thickness in the magnetosphere side (Dimmock et al., 2015; Henry et al., 2017; Nykyri & Dimmock, 2016; Nykyri & Otto, 2001). In this scenario, the investigation of the suitable conditions for the KH growth in the near-Earth environment, through global MagnetoHydrodynamic (MHD) simulations, has shown that higher values of the solar wind speed produce higher velocity shears at the magnetopause which can enhance the KH instability (W. Y. Li et al., 2012). Conversely, depending on the solar wind magnetic field orientation, one of the two magnetopause flanks can undergo a higher magnetic compression, which can suppress the instability (Nykyri, 2013).

In the framework of *in situ* observations, an aspect of the KH instability that is currently unclear is related to the identification of its evolutionary stage and vortex boundaries. MHD simulations showed that rolled-up vortices are characterized by lower density and faster plasma than is observed in the magnetosheath regions (Takagi et al., 2006). Although such a trend has been found in several KH events observed at the Earth's magnetopause, it does not uniquely characterize KH vortices but can denote different phenomena, such as plasma depletion layers (Plaschke et al., 2014). Plaschke et al. (2016) suggested a tool for the identification of KH vortices, based on the angle between the propagation direction of the observed structure and the vector normal to the boundary. A different orientation of the normal to the boundary indicates whether a wave, a KH wave, or a KH vortex is crossed. However, this method requires multi-spacecraft measurements to perform timing analysis on the boundaries and is not able to distinguish between KH vortices in the early nonlinear stage and rolled-up vortices which develop during the fully nonlinear phase.

In this work, we propose a new parameter based on single-spacecraft particle measurements to identify KH vortices and their evolutionary stage. Specifically, such a parameter quantifies the degree of mixing for particle populations of the same species with distinct temperatures and energies. The Earth's magnetopause is the perfect candidate for this method since the magnetospheric and magnetosheath plasmas interacting at the magnetopause typically have distinct properties that make them clearly distinguishable. We apply our analysis to a specific KH event, during which MMS recorded a continuous period of high-resolution burst mode data at the dusk flank close to the equatorial plane. The outline of the paper is the following: in Section 2 we provide a brief overview of the KH event, describing the main features and the coordinate system used; in Section 3 we introduce the mixing parameter for spacecraft measurements and we show three particular crossings, which correspond to a different shape in the mixing parameter-space; in Section 4 we perform a statistical analysis of the KH crossings,

suggesting a transition from linear to steepened waves and eventually rolled-up vortices. In Section 5 we discuss the solar wind conditions that lead to the enhancement of the KH instability and, finally, in Section 6 we state the conclusions.

2. MMS Observation of Kelvin-Helmholtz Instability

We analyze data from the MMS1 spacecraft. We show the magnetic field data from the FluxGate Magnetometer (Russell et al., 2016), sampled at 16 Hz in fast mode and 128 Hz in burst mode, and the particle data collected by the fast plasma investigation instrument (Pollock et al., 2016) with a cadence of 4.5 s in fast mode and 150 ms (30 ms) in burst mode for ions (electrons).

2.1. Overview of the Event

On 8 September 2015, during an outbound magnetopause crossing, MMS observed more than 1 hr of periodic or quasi-periodic fluctuations at the dusk flank magnetopause before the terminator. Such perturbations were identified as surface waves excited by the KH instability (see Eriksson et al., 2016; W. Li et al., 2016 for further details). During the interval 09:00 - 09:21 UTC, the spacecraft was in the magnetosphere and exited into the pure magnetosheath after 11:27 UTC. Figure 1g shows the MMS trajectory (green curve), during which the satellite moved from [5.19 7.19 0.23] R_E in geocentric solar ecliptic (GSE) coordinates to [4.73 9.64 0.03] R_E, about 3 R_E away from the nose of the Earth's magnetopause.

We show an overview of the MMS observations in panels (a)-(f). The beginning and final part of the interval is characterized by an unperturbed plasma. During the first ∼20 min, MMS1 observed a hot and low density plasma characterized by an approximately zero plasma flow consistent with the pure magnetosphere (MSP). During the last ∼3 min, MMS1 observed a cold and dense plasma characterized by a high speed flow which indicates the pure magnetosheath (MSH). In between the spacecraft encountered ∼2 hr of quasi-periodic fluctuations where the cold dense MSH plasma coexists with the hot magnetospheric one. These perturbations are clearly observed in several quantities, namely, both the ions and electrons energy spectrograms, E_i, E_e (panels a and b), the ion density, N (panel c), and the ion and electron temperatures, T_i and T_e (panel d). While E_i displays only two populations (the magnetospheric and magnetosheath ions) which mix in correspondence of the periodic perturbations, E_e shows three different populations of electrons, namely the expected MSP and MSH electrons, and a third population with intermediate density and temperature with respect to the MSP and MSH, in the energy range [200 1000] eV. This intermediate population constitutes a preexisting boundary layer (BL) that could have been originated from magnetic reconnection events (Vernisse et al., 2016).

In panels (e) and (f) both the magnetic field and ion bulk velocity are shown in a local boundary coordinate system (*lmn*), which will be discussed in Section 2.2. The $\hat{\mathbf{m}}$ and $\hat{\mathbf{n}}$ versors are illustrated in Figure 1g: $\hat{\mathbf{m}}$ is approximately tangential to the flank of the magnetopause, while $\hat{\mathbf{n}}$ is normal to the boundary and directed outward. In the first part of the perturbed interval we observe ion velocity fluctuations with an average value around zero; while in the second part V_m displays fluctuations with an average value of 200 km s^{-1}, consistent with the MSH crossing (panel f). Moreover, a clear shear flow is observed along the m-direction with a jump of about 400 km s^{-1} or 1.1 V_A (V_A being the Alfvén speed in the MSH). Finally, the magnitude of $\mathbf{B}$ is mostly given by the B_l component, while B_n and B_m are close to zero but, during the KH interval, they display bipolar changes, which correspond to boundaries and narrow current sheets.

2.2. *lmn* Coordinate System

We rotate the GSE coordinate system into a local boundary normal system, *lmn*, to better describe the physics of the event. We take $\hat{m}$ along the direction of the KH wave vector, $\mathbf{k}$; $\hat{l}$ in the direction of the averaged magnetic field evaluated in the MSP and MSH, and finally, $\hat{n}$ completes the right hand orthonormal basis and it is evaluated as $\hat{\mathbf{n}} = -\hat{\mathbf{l}} \times \hat{\mathbf{m}}$ in order to take the outward direction with respect to the magnetopause. To ensure the orthogonality of the coordinate system, we fixed the $\hat{\mathbf{m}}$ and $\hat{n}$ unit vectors and evaluated $\hat{l}$ as the cross product ($\hat{\mathbf{l}} = \hat{\mathbf{m}} \times \hat{\mathbf{n}}$). We point out that, since the total magnetic field is almost uniform along the whole interval, $\hat{l}$ indicates the minimum variance direction.

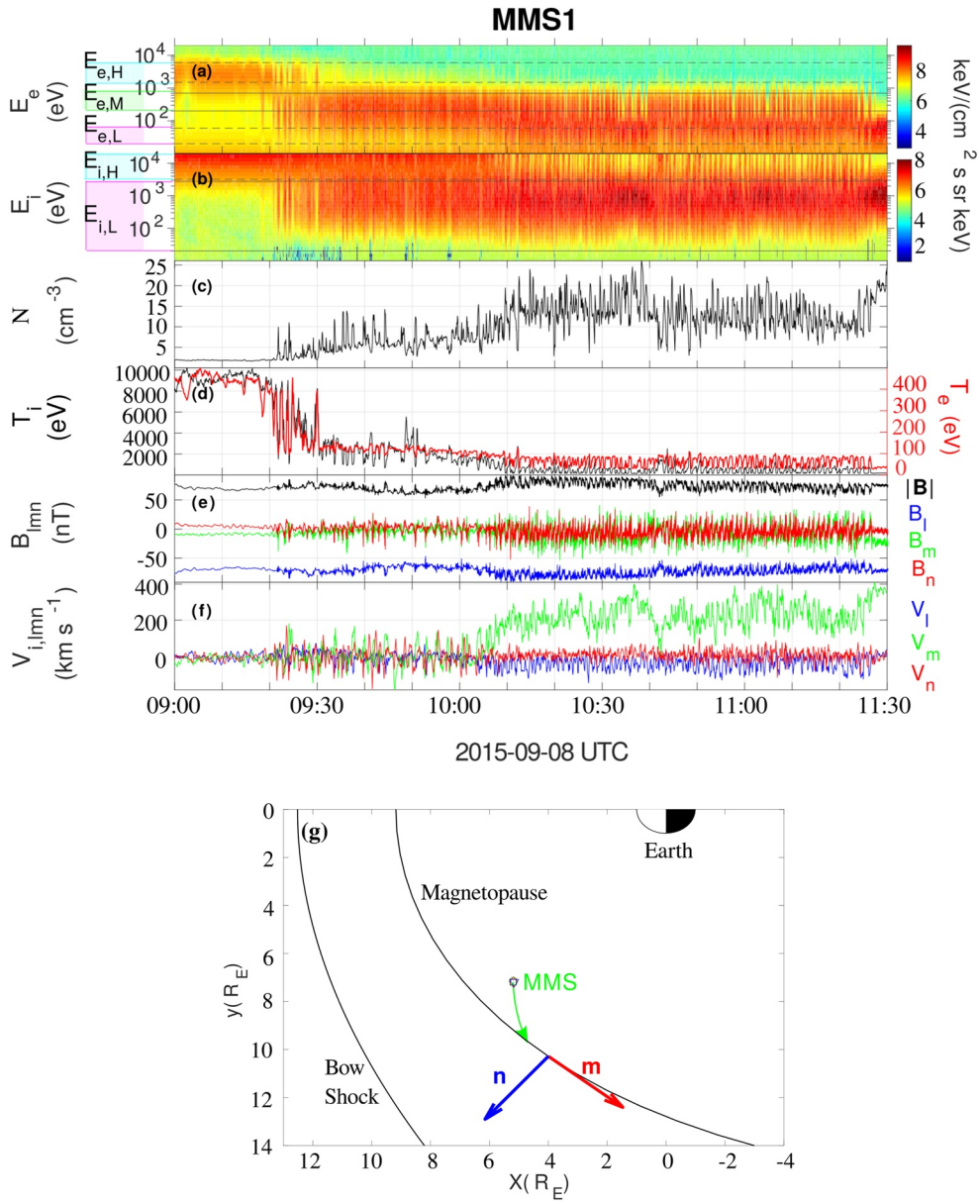

Figure 1. Overview of the Kelvin-Helmholtz (KH) event observed by magnetospheric multiscale (MMS) 1 from 9:00:00 to 11:30:00 UTC on 8 September 2015. From top to bottom: (a) ion energy spectrogram, (b) electron energy spectrogram, (c) ion density, (d) ion (black curve) and electron (red curve) scalar temperatures, (e) magnetic field rotated to the local boundary coordinate system (*lmn*) described in the text, (f) ion bulk velocity in *lmn* coordinates. (g) Schematic showing the dusk side of the near Earth's environment in the GSE *xy* plane. The green curve indicates the MMS trajectory, while the red and blue arrows are the in-plane unit vectors of the local boundary coordinate system.

The direction of **k** is evaluated from the linear dispersion relation for an incompressible plasma (Chandrasekhar, 1961)

$$\omega = \frac{\mathbf{k}\cdot(\rho_1\mathbf{V}_1+\rho_2\mathbf{V}_2)}{\rho_1+\rho_2} \pm i\sqrt{\frac{\rho_1\rho_2}{(\rho_1+\rho_2)^2}[\mathbf{k}\cdot(\mathbf{V}_2-\mathbf{V}_1)]^2-\frac{1}{\mu_0(\rho_1+\rho_2)}[(\mathbf{k}\cdot\mathbf{B}_1)^2+(\mathbf{k}\cdot\mathbf{B}_2)^2]}, \quad (1)$$

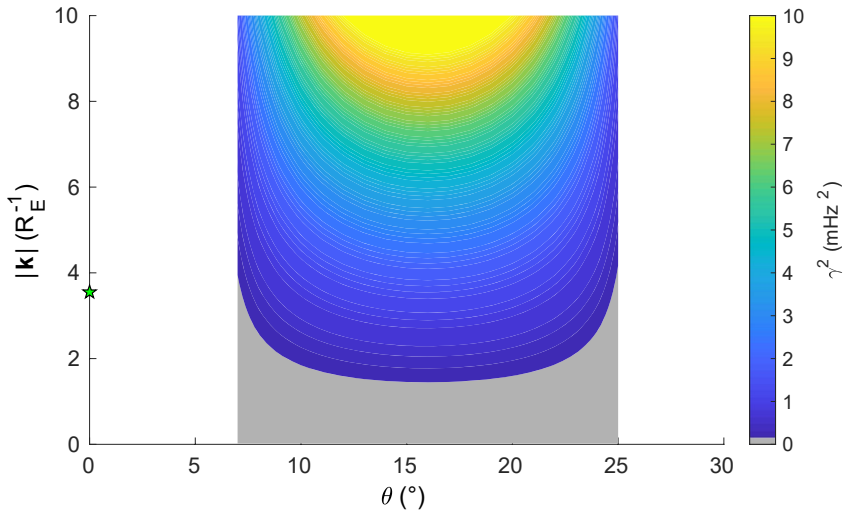

Figure 2. Contour-plot of the squared Kelvin-Helmholtz growth rate evaluated from the imaginary part of Equation 1, γ^2, in the function of the wave number, $|\mathbf{k}|$, and the angle between the wave vector and the mean ion bulk velocity direction, θ. The green star corresponds to the wavenumber, which is obtained by performing timing analysis on the magnetic field.

where $\rho_{1(2)}$ is the average mass density, $\mathbf{V}_{1(2)}$ is the bulk flow, $\mathbf{B}_{1(2)}$ is the magnetic field, the subscript 1(2) refers to the MSP (MSH), and μ_0 is the magnetic permeability. Equation 1 indicates that the plasma is unstable to the KH instability when the imaginary part, γ, is strictly greater than 0 ($\gamma > 0$).

In Figure 2 we have analyzed the behavior of γ^2 for several values of the wave number, $|\mathbf{k}|$ and θ, which is the angle between $\mathbf{k}$ and the mean bulk velocity. We observed that the magnetopause is stable to the KH for any value of the wave number when $\mathbf{k}$ is assumed to be exactly along the shear ($\theta = 0°$). However, positive growth is obtained only for the ranges $\theta = [8°, 25°]$ and $\theta = [188°, 205°]$ (not showed because the KH waves propagate tailward). In this approximation, we observe that the instability grows for increasing wave numbers and the region of positive growth only depends on angles. Thus, to evaluate the direction of the wave vector and consequently of $\hat{m}$, we take the averaged direction in the unstable region. We obtained the following unit vectors in GSE coordinate system: $\hat{\mathbf{l}} = [-0.17\ \ -0.11\ \ -0.98]$, $\hat{\mathbf{m}} = [-0.76\ 0.64\ 0.06]$, $\hat{\mathbf{n}} = [0.62\ 0.76\ \ -0.19]$.

3. Mixing Parameter

In this section, we present a statistical analysis of the KH event using the mixing parameter, which quantifies the degree of mixing between magnetospheric and magnetosheath plasmas and provides information about the topology of the magnetic field lines. A similar parameter has been used in simulation data to identify the topology and evaluate the reconnection rate (Daughton et al., 2014; Nakamura & Daughton, 2014). Contrary to numerical simulations, where we can keep track of the particle's trajectory, for, *in situ* measurements, we cannot have full control of where particles are coming from. However, as the energies in the particles in the MSP and MSH are so distinct, we can use particle energies to distinguish between different populations. Thus, we define the mixing degree for both electrons and ions based on the different particles' energies highlighted by the colored rectangles and horizontal lines in panels (a) and (b) of Figure 1. The mixing parameter is defined as:

$$\mu_\alpha = \frac{\sigma_{\alpha,a} - \sigma_{\alpha,b}}{\sigma_{\alpha,a} + \sigma_{\alpha,b}}, \tag{2}$$

$$\sigma_{\alpha,a(b)} = \int_{E_{\alpha,a(b)}} f_\alpha(E,t)\, dE, \tag{3}$$

where $\sigma_{\alpha,a(b)}$ is the omnidirectional particle distribution function, $\alpha = i, e$ the index running on the particle species, and a and b the energy ranges of the integral indicated in Figures 1a and 1b. Specifically, the ion mixing, (μ_i), is defined by using two different energy ranges: (a) the high-energy range, $E_{i,H}$ (magenta shaded region in Figure 1b), for the MSP; (b) the low-energy range, $E_{i,L}$ (cyan shaded region in Figure 1b), for the MSH. For the electrons,

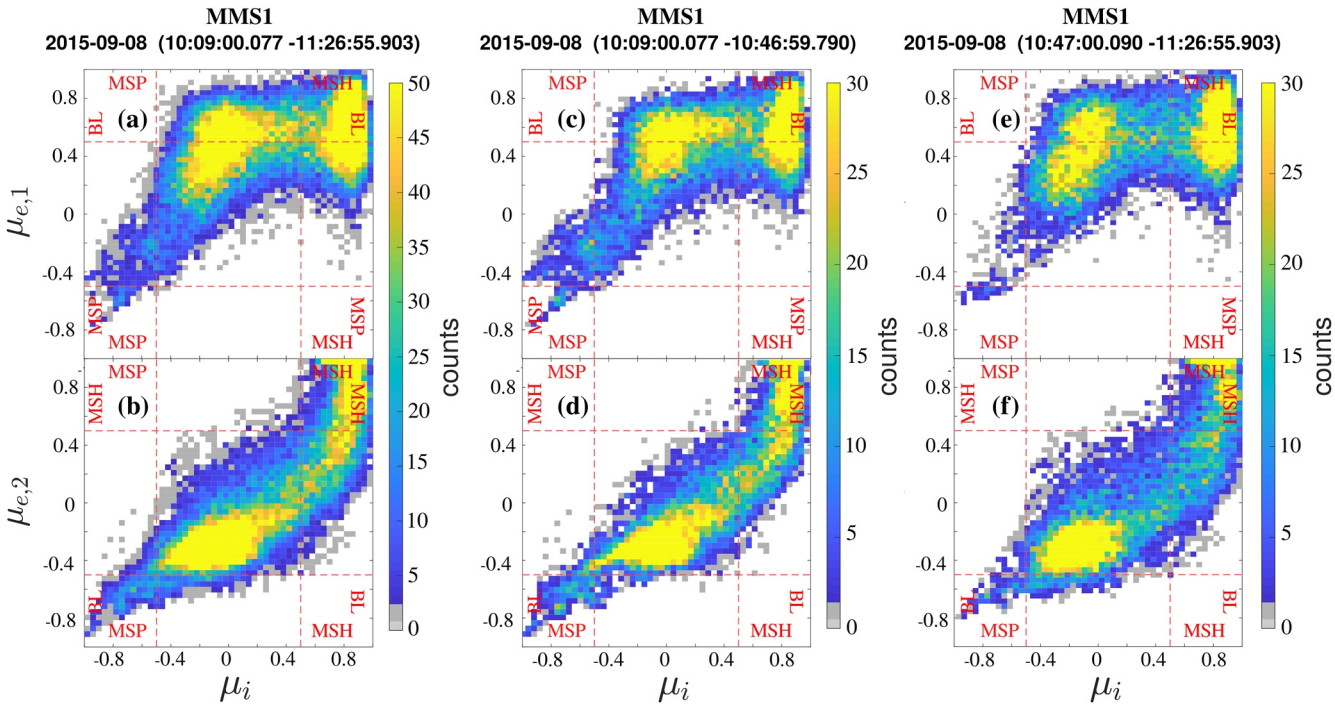

Figure 3. 2D histograms of μ_α illustrated in each of the two mixing parameter-spaces: [μ_i, $\mu_{e,1}$] (top panels) and [μ_i, $\mu_{e,2}$] (bottom panels) for three different time intervals. From left to right, the time intervals are the whole Kelvin-Helmholtz event, the first half of the event, and the second half.

three populations are resolved in the spectrogram, so we define two different electron mixing parameters, namely $\mu_{e,1}$ and $\mu_{e,2}$, by using the three energy ranges highlighted in Figure 1a. On the one hand, $\mu_{e,1}$ is defined by the high ($E_{e,H}$, cyan shade) and intermediate ($E_{e,M}$, green shade) energy ranges, that identify the MSP and BL, respectively; on the other hand, $\mu_{e,2}$ is defined by the intermediate and low energy ($E_{e,L}$, magenta shade) ranges, which indicate BL and MSH populations, respectively.

Both electron and ion mixing parameters are normalized quantities and range between -1 and 1. In the upper limit ($+1$) the low-energy population dominates, while in the lower limit (-1) the high-energy population dominates. For example, for μ_i the limits -1, $+1$ correspond to the pure MSP and MSH, respectively. Despite the same definition, the electron and ion mixing parameters have different physical meanings. The former provides information about the topology of the magnetic field, while the latter is connected to the level of mixing of the plasmas on the two sides of the magnetopause. Indeed, since electrons move faster than ions along magnetic field lines, electron mixing can be used to distinguish topologically connected regions and to detect boundaries characterized by sharp gradients.

We study μ_α in each of the two parameter-spaces generated by μ_i with $\mu_{e,1}$, and μ_i with $\mu_{e,2}$, respectively. Figure 3 shows the counts of μ_α in both the mixing parameter spaces for different time intervals, namely, the whole KH interval (left), the first half (center), and the second half of the event (right). Moreover, we define a threshold for the ions mixing (vertical dashed lines) and electrons mixing (horizontal dashed lines) which distinguishes the mixed region (central square) from the high-energy and low-energy regions. In such a mixing parameter-space, the top right region indicates the low-energy population for both ions and electrons, while the bottom left region corresponds to the high-energy ions and electrons. According to our definition of $\mu_{e,1}$ and $\mu_{e,2}$, the high (low)-energy region coincides with the pure MSP (MSH) only in the parameter-space [μ_i, $\mu_{e,1}$] ([μ_i, $\mu_{e,2}$]). In the other cases, the BL electrons are also involved.

The different parts of these parameter spaces provide information about the plasma properties and the magnetic field lines. If we move vertically down (meaning we fix a value for the ion mixing parameter), the electron mixing is the only one varying. Since electrons move faster than ions along the magnetic field, such a change in the electron mixing only would indicate that the plasma properties stay the same, but the magnetic field lines are distorted and connected to topologically different regions (the high- and low-energy regions). This change in

the connectivity allows the low-energy electrons to penetrate inside the high-energy region. On the contrary, if we move horizontally, only the ion mixing varies, suggesting that regions with the same topology, but different plasma properties, are crossed. In all the panels, from right to left, we first encounter the low-energy unperturbed ions, then after the first ion threshold, increasingly high-energy ions come into play, indicating the crossing of a mixed plasma, and finally, after the second ion threshold, we exit into the unperturbed high-energy side. The top panels in Figure 3 show that the majority of the counts are localized in two main blobs corresponding to the low-energy population (close to [1, 1]) and a more mixed region (close to the center). Panel (a) shows that the transition between these two plasmas, from right to left, is relatively flat at the beginning, thus suggesting the crossing of regions with similar topologies. Close to $\mu_i = 0$, instead, we observe a hard break indicating a sudden transition from two topologically different regions due to highly distorted magnetic field lines. Moreover, few counts are detected in the pure MSP owing to a more mixed plasma. It is worth pointing out that low-energy particles are observed in the high-energy region (about $[-0.8, -0.3]$) due to finite gyroradius effects. The finite Larmor radius effect is observed only at the beginning of the event (panel c), while at late times there is no clear evidence (panel e), probably due to the enhancement of counts in the mixed region. In addition, there are relatively few counts in the high-energy region with respect to the beginning of the interval, which further suggests the higher degree of plasma mixing.

In the bottom panels, the counts fill the mixing parameter space from the top right side to the bottom left. The overall event shows a high number of counts all along the region from the low to the high energy side. The same trend is also observed at the beginning of the interval (panel d), while at the end (panel f) the transition is sharper, and particles are mainly localized in two groups. Moreover, we observe a spreading of the shape and fewer counts in the high-energy region during the very last part of the interval compared with the beginning.

Besides this statistical analysis, we can also study in detail the trajectories in the mixing parameter-space for the individual crossings of the structures. For each crossing we observed that the same trajectory was recovered in the parameter-space $[\mu_i, \mu_{e,1}]$; while for $[\mu_i, \mu_{e,2}]$ the mixing parameter followed different trajectories. We could distinguish three main trajectory types in this parameter space which, as we will discuss in Section 4, likely correspond to different structures, namely linear waves, steepened waves, and rolled-up vortices. In the following subsections, we present three particular crossings, indicated as Type I, Type II, and Type III, which are representative of each group.

3.1. Type I Crossing—Linear Wave

First, we consider the simplest type of crossing observed in the mixing parameter-space, which is when the same trajectory is followed for both the inbound and outbound parts of the crossings. Such a symmetry implies that there is no difference in the boundary structure when the spacecraft is moving in or out, which corresponds to a linear wave.

In Figure 4, the ion energy spectrogram (panel a) displays two different regions. We observe a transition from the MSH plasma to a mixed region (between 10:33:45 - 10:34:05 UTC), where both high- and low-energy populations are detected, and then back to the MSH plasma between 10:34:05 - 10:34:15 UTC. The electron spectrum, instead, displays three different regions. First, we observe a transition from MSH electrons to BL (between 10:33:40 - 10:33:45 UTC) where high and low energy electrons coexist but the low-energy are the predominant ones, and then we cross a mixed region (between 10:33:45 - 10:34:05) where the high-energy electrons dominate. Finally, we go back into the MSH after crossing the BL region again. The temperatures, which are plotted on top of the particle spectra (black lines) are also consistent with such observations since they increase both at the BL and the mixed region. The origin of the BL may be connected to mid-latitude reconnection. Indeed, the electron pitch angle distribution (not shown) displays a flux of middle-energy electrons (between 200 and 700 eV) coming predominantly from the parallel direction. We observe that overall this crossing is very symmetric, that is, the electron energy spectrogram shows two similar BL on both sides of the mixed region.

The same boundaries and regions are also identified by the mixing parameters, $\mu_{e,2}$, μ_i (panel c). Right before and after the mixed region, μ_i stays constant and close to 1, indicating an MSH plasma; while $\mu_{e,2}$ starts to decrease, which indicates a topologically different region is encountered characterized by high-energy electrons and a dominant intermediate energy population corresponding to the BL. Inside the mixed region, both μ_i and $\mu_{e,2}$ are

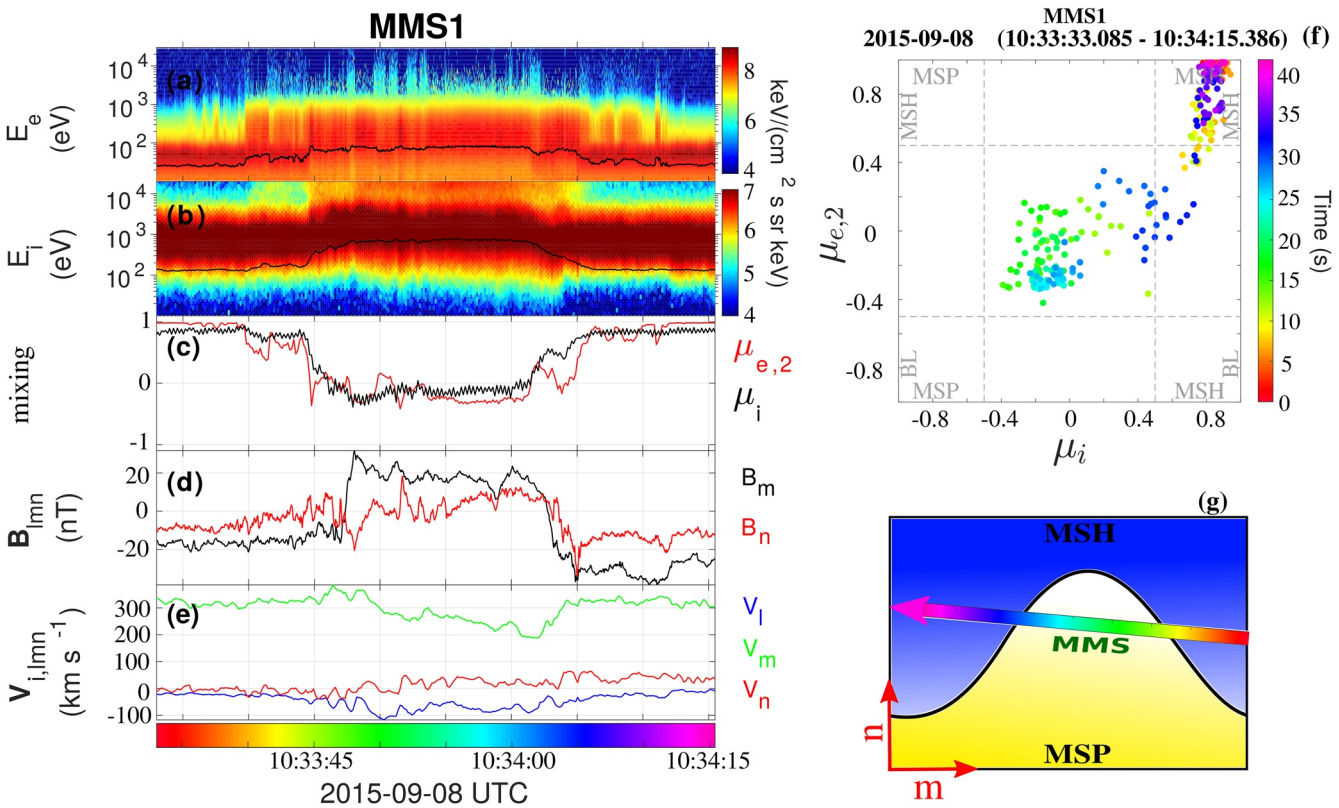

Figure 4. Magnetospheric multiscale (MMS) 1 data from 10:33:33 to 10:34:15 UTC on 8 September 2015, corresponding to the crossing of a linear Kelvin-Helmholtz wave: (a) electron energy spectrogram; (b) ion energy spectrogram; (c) electron and ion mixing parameters, μ_i and $\mu_{e,2}$ defined in Equations 2 and 3; (d) in plane components of the magnetic field in the *lmn* system; (e) ion bulk velocity in the *lmn* coordinate system; (f) trajectory in the parameter-space generated by [μ_i, $\mu_{e,2}$]. The colorbar indicates the time in seconds and provides the direction of the trajectory since the start of the interval; (g) sketch of the MMS crossing. The blue and yellow colors represent the MSH and pure magnetosphere, respectively, and the black curve the boundaries of the structure. The arrow indicates the trajectory of the satellite.

mostly negative. Such behavior indicates that changes in the mixing parameters nicely reflect the electron and ion boundaries which we identify by eye in the electron and ion spectra.

Then, we look at the magnetic field and the ion bulk velocity. Since B_l is quite constant along the whole interval (see Figure 1d), we will only focus on the m and n components. Panel 4d shows that both magnetic field components are negative in the MSH. In panel (e) we show the ion velocity components in the *lmn* coordinate system. The main contribution comes from V_m (green curve) which is close to the direction of the shear flow. V_m approaches 400 km s^{-1} in the MSH and decreases to $\simeq$200 km s^{-1} in the mixed region. At both ion boundaries, we observe clearly symmetric boundaries in B_m component, suggesting the crossing of two similar current sheets.

In Figure 4f we plot the electron mixing parameter $\mu_{e,2}$ as a function of the ion mixing parameter μ_i. The colors indicate the time since the start of the interval and provide the direction of the trajectory in the mixing parameter-space. The trajectory starts at about [1, 1] (red color coding) and, after crossing the first electron threshold (horizontal dashed line at 0.5), becomes oblique crosses the ion threshold (vertical dashed line at 0.5) and enters into the central zone of the diagram where MSH and MSP plasmas are mixed. We note the large distance between the data points in the green interval, corresponding to a fast motion in the mixing parameter-space, which suggests the crossing of narrow current sheets. Then, the trajectory reverses and follows the same path as the inbound one. Indeed, the fast motion in the blue part of the trajectory is observed in the same region as before (green), indicating a certain symmetry in the structure crossed by the spacecraft, that is, the similarity of the boundaries encountered during the inbound and outbound crossings.

This symmetric trajectory in the mixing parameter-space likely corresponds to the crossing of a linear wave as illustrated by the sketch in Figure 4g. The blue and yellow regions correspond to the MSH and MSP, which are separated by the current sheet (black line); the lighter region close to the boundary indicates the mixed region.

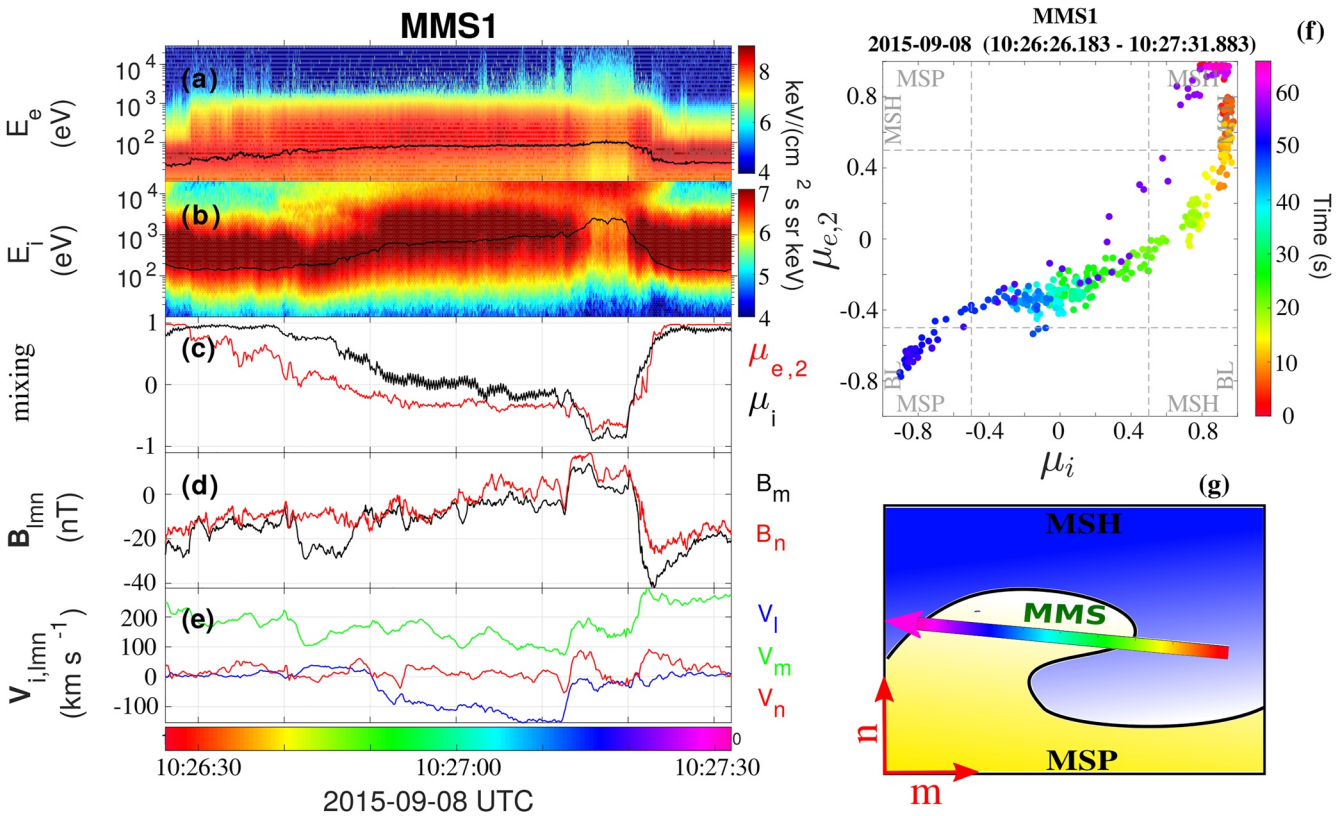

Figure 5. Magnetospheric multiscale 1 data from 10:26:26 to 10:27:31 UTC on 8 September 2015, corresponding to the crossing of a steepened wave. The same quantities as in Figure 4 are shown.

First, MMS encounters the pure MSH plasma (blue region), then it crosses the boundary for the first time, which corresponds to a fast motion in the mixing parameter-space, and finally, enters into the mixed region dominated by the plasma of magnetospheric origin (light yellow). There are no data points in the high-energy region of the mixing parameter-space $[-1, -1]$, which can be interpreted as MMS passes really close to the crest of the wave. Finally, MMS crosses the boundary for the second time and exits back into the MSH (blue region). All the crossings of this type display similar inbound and outbound trajectories in the mixing parameter-space, but in some cases we also observe data points in the high-energy region ($[-1, -1]$), if MMS is crossing far from the crest where the plasma is not mixed.

3.2. Type II Crossing—Steepened Wave

The second type of crossing is characterized by a substantial difference for the inbound and outbound trajectories in the mixing parameter-space. This suggests a crossing of an asymmetric structure, which would correspond to a steepened wave. Figure 5 shows an overview of such an asymmetric crossing. The ion energy spectrogram (panel b) displays cold and dense ions until the crossing of the first ion boundary at 10:26:40. After this time, MMS encountered a mixed region, which is characterized by both high and low energy ions. However, the energy spectrum is dominated first by the low energy population but then, approaching the second ion boundary, the high energy population becomes dominant. Finally, before the exit into the proper MSH at 10:27:25 UTC, for a few seconds, we observe two populations of ions with different energies. The ion temperature, which is plotted on top of the ion spectrum (black curve), shows the same behavior. It smoothly increases after the first ion boundary, peaking in the mixed region where the high energy population dominates; but then suddenly decreases in correspondence of the other ion boundary. Besides the three main regions discussed above for the ion spectrum (MSH, the two mixed regions dominated by the low or high energy population), in the electron spectrum (panel a) we also observe a BL in correspondence with both the ion boundaries but outside the mixed region. The first ~5 s of the interval, which are characterized by an MSH plasma, are followed by 10 s of BL, where the high

energy population becomes increasingly important and the dominant one inside the mixed region. Indeed, in correspondence with the second ion boundary, on the left side, we observe high-energy electrons (above 2 keV). The electron pitch angle distribution (not shown) shows that such a long-duration BL is filled with middle energy electrons coming primarily from the antiparallel direction, thus suggesting a connection between magnetospheric and magnetosheath field lines at mid-latitude. On the right side of the second ion boundary, we encounter a small region of BL before exiting into the MSH. The different extent of the BL on each side of the mixed region highlights the above-mentioned asymmetry of the structure.

Contrary to what is observed for the linear crossing (Figure 4), where both ion boundaries are sharp, the present crossing is characterized by a rather smooth inbound transition into the mixed region and a sharp outbound crossing. We can further investigate the boundaries using the mixing parameters (panel c). At the beginning of the interval, μ_i remains close to 1, while $\mu_{e,2}$ decreases, indicating a change in the connectivity of the magnetic field lines. After the first ion boundary, both mixing parameters decrease approaching -1, which indicates a hot magnetosphere-like plasma. However, $\mu_{e,2}$ is consistently lower than μ_i for the inbound crossing, while the two mixing parameters are similar for the outbound part. Such observations suggest that MMS is crossing an asymmetric structure. We also observe a similar asymmetry in the behavior of the magnetic field and the ion bulk velocity (panels d and e). At the first ion boundary, B_m and B_n display a gradual transition from negative to positive values; but, in correspondence with the second ion boundary, both the field components show a strong bipolar structure, which indicates the crossing of a narrow current sheet. An asymmetric profile is also observed for V_m inside the mixed region since it is gradually decreasing on the inbound side and sharply increasing on the outbound part.

In Figure 5f we show the trajectory in the mixing parameter-space for the present crossing. We can observe some similarities with the linear case. The trajectory starts in the high energy part of the diagram ([1, 1]) and moves vertically down (red and orange intervals) crossing the first electron threshold (first horizontal dashed line). Then the trajectory becomes curved since both μ_i and $\mu_{e,2}$ are decreasing. The central region is characterized by a smooth and continuous transition until the second ion threshold where the trajectory steepens, owing to the penetration of low energy plasma in the MSP side due to finite gyroradius effects. Then, the trajectory reverses but follows a different path with respect to the inbound crossing. Along this path, we observe the high distance between the data points (violet interval), which corresponds to a fast movement in the mixing-parameter space. Such a feature occurs due to the current sheet associated with the bipolar magnetic field, as discussed above. Thus, the trajectory in the mixing-parameter space can capture pretty well all the boundaries and allows us to distinguish the different regions of the plasma.

Our interpretation is that MMS is crossing an asymmetric structure that nicely corresponds to a steepened wave (see the sketch in Figure 5g). Indeed, the centrifugal force acts to confine the low-density plasma close to the leading edge of the vortex and at the same time leads to the mixing of plasmas on the two sides. This results in a smoother transition from MSH to MSP as well as a shallower boundary at the leading side (first ion boundary). On the other hand, the trailing edge of the vortex (second ion boundary) results in a steeper boundary and a sharp transition from the mixed region into the MSH.

For Type I crossings we expect the leading and trailing edges to be similar (symmetric), while for Type II crossings we expect a smooth leading edge and a steep trailing edge. However, we encountered several marginal cases between two different groups of shapes. To classify them, we checked whether any degree of symmetry could have been recovered in the magnetic field and the energy spectrogram. In particular, we considered the duration of the current sheet at both the leading and trailing edges of the structure. We categorized as Type II crossings those showing the shallower leading boundary and a very sharp trailing boundary lasting less than 5 s.

3.3. Type III Crossing—Rolled-Up Vortex

The last type of crossing is the most complex since the trajectories in the mixing parameter-space for the inbound and outbound crossings are completely different and highly complicated. This implies that the boundaries of the structure are quite distorted and any degree of symmetry has disappeared, which suggests the crossing of a rolled-up KH vortex. The overview plot in Figure 6 shows a clear MSH plasma during the initial and final parts of the interval; while in between (central interval), the plasma is highly dynamic and variable. In such a region, the electron and ion energy spectrograms (panels a and b) continuously change intensities in both the high and low energy ranges and the particles' temperature displays several local maxima and minima. In contrast to the other

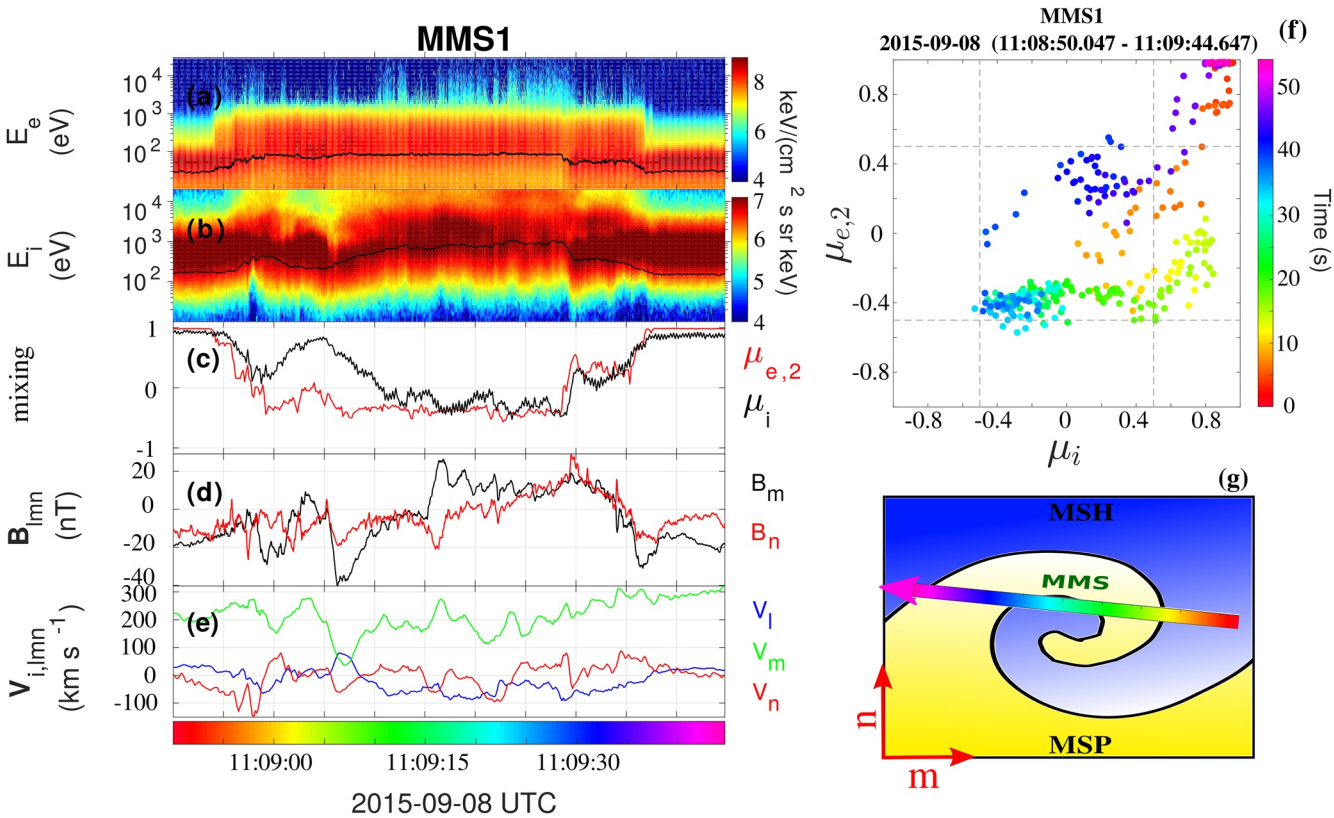

Figure 6. Magnetospheric multiscale 1 data from 11:08:50 to 11:09:44 UTC on 8 September 2015, corresponding to the crossing of a rolled-up vortex. The same quantities as in Figure 4 are shown.

crossings, μ_i is not decreasing monotonically but displays an enhancement in the time interval between 11:09:00 UTC and 11:09:10 UTC. In correspondence with this interval, the magnetic field is also varying a lot and shows the presence of several boundaries, particularly evident in the B_m component (panel d). The same complex behavior can be recognized in the ion bulk velocity (panel e), whose components are highly fluctuating.

This highly dynamic behavior results in a highly complex shape in the mixing-parameter space (see Figure 6f). The trajectory starts at [1, 1] (low energy side) and quickly reaches the central part of the diagram following an oblique path (red and orange data points), indicating that both ions and electrons species are rapidly changing. Then, the trajectory suddenly turns around on a different path and crosses the ion threshold at $\mu_i = 0.5$ for the second time (yellowish and green interval). The twist of the trajectory occurs in correspondence with the strong bipolar magnetic field component B_m (panel d), suggesting the crossing of a highly distorted structure. In the green and cyan intervals, the trajectory enters again the central region but along a different path. We note that the inbound trajectory does not exit into the high energy side probably because of a highly mixed plasma. Finally, the outbound trajectory follows a different path with respect to the inbound and displays a very fast transition from the high-to the low-energy regions, as indicated by the large distance between data points. During this fast movement in the mixing parameter-space, both the magnetic field components are sharply changing signs, which indicates the crossing of a narrow current sheet.

Due to the high complexity of the shape, as well as the presence of twists and sudden changes in the trajectory direction, this crossing can be reasonably interpreted as a rolled-up vortex (see sketch of the crossing in Figure 6g). Rolled-up vortices are typically observed during the late nonlinear stage of the KH instability when the two plasmas are highly mixed and the magnetic field lines are stretched and twisted due to the vortical flow. Such rotating motion of the plasma can lead to the formation of small islands containing MSH-like plasma within the mixing region. Such an island can be seen for example, in Figure 6 at 11:09:05 UTC. Therefore if during the crossing the ion mixing parameter goes up and down (once or several times) assuming both positive and negative values we interpret such crossing as a Type III.

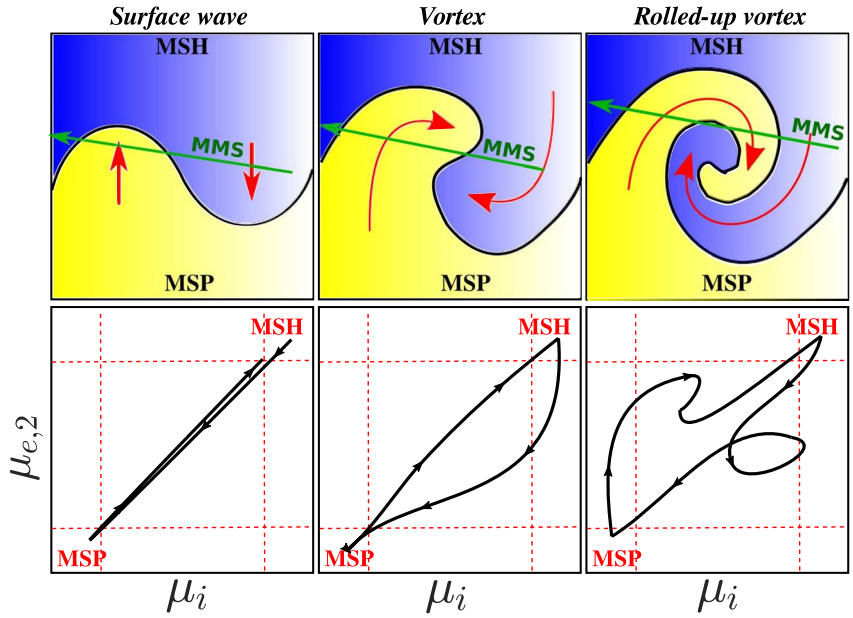

Figure 7. Top: sketches of the magnetospheric multiscale (MMS) 1 crossing of the linear wave (left), steepen wave (center), and rolled-up vortex (right). The dark blue and yellow regions are the pure magnetosheath and pure magnetosphere, while the light colors indicate a mixed region. The green arrow indicates the MMS1 trajectory across the structure, whose boundaries are represented by the black curve. Finally, the two red arrows indicate the direction of the pressure gradients. Bottom: Corresponding trajectories for each type of crossing observed in the mixing parameter-space.

4. Statistical Analysis

In this section we summarize our interpretation of the different trajectories in the mixing parameter-space and provide a statistical analysis of the shapes observed in the whole KH interval.

4.1. Summary of the Crossings

Figure 7 shows schematically the structures observed by MMS along with the suggested trajectory of the satellite (top panels), and the corresponding trajectory in the mixing parameter-space [μ_i, $\mu_{e,2}$] (bottom panels). During the linear phase of the KH instability (left panels), surface waves are generated, which propagate from the nose toward the tail along the flank of the magnetopause. For these conditions, the plasma interacting at this interface starts to mix, generating a layer of plasma with intermediate properties (density, temperature, and energy) between the MSP and MSH. However, the degree of mixing is quite low and far away from the interface, such waves are characterized by non-mixed original plasmas. Moreover, the boundaries of the waves are equally steepened on both sides. These properties are in agreement with the observed trajectory in the mixing parameter-space, which is the same during both the inbound and outbound crossings. It is worth pointing out that if the satellite is crossing the linear wave far from the crest, the trajectory in the mixing parameter-space would exit in the high energy region (close to $[-1, -1]$).

During the early nonlinear stage of the instability (middle panels), the pressure gradient (red arrows) and the centrifugal force tends to confine the low density (magnetospheric) plasma at the center of the vortex, close to the leading edge, which creates sharper (smoother) boundaries on the trailing (leading) edge. Then, the vortical plasma flow leads to the distortion of the magnetic field lines, which are steepening on the trailing side. Thus, the resulting trajectory in the mixing parameter-space is different for the inbound and outbound crossing, as shown in Figure 7 (bottom middle panel). Since the higher degree of mixing occurs at the leading edge of the vortex, the inbound trajectory is a curved line which indicates a shallower and smoother transition from the low to the high energy sides. On the contrary, the outbound trajectory is characterized by a straight line, which indicates a fast displacement from the high to the low energy side. Such a fast transition is connected to the crossing of strong boundaries in the magnetic field lines, which corresponds to narrow current sheets.

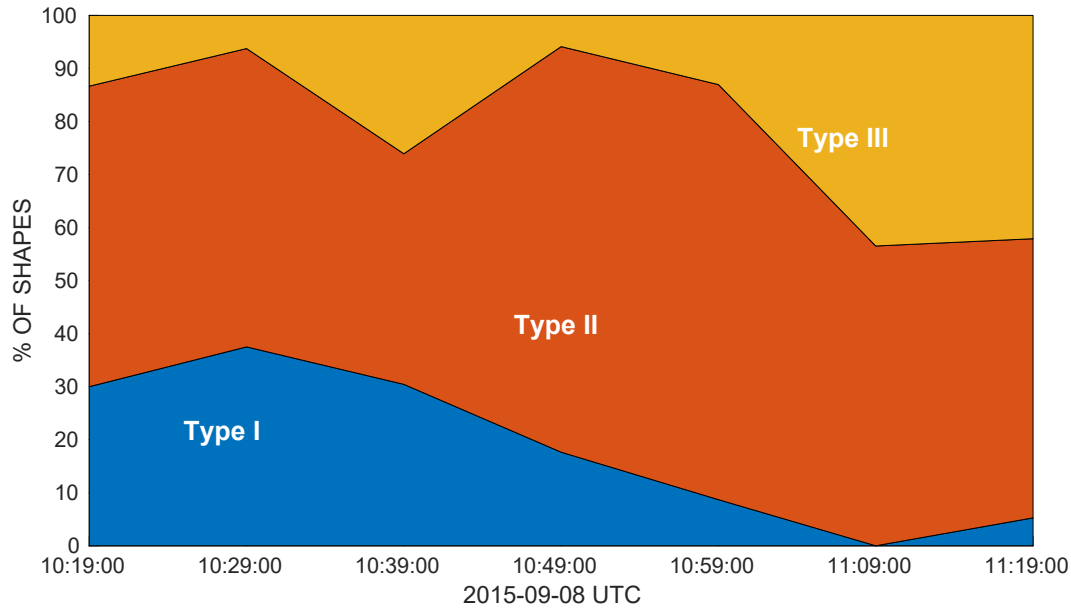

Figure 8. Percentage of each of the three types of shapes (straight line, simple loop, complex loop) schematized in Figure 7 evaluated in 20 min intervals during the whole Kelvin-Helmholtz event. The number of a specific type of shape in each interval is normalized to the total number of shapes in that interval. The times on the *x*-axis are the central time of the 20-min interval. Finally, the colors indicate Type I (blue), Type II (red), and Type III (yellow) groups, whose corresponding structures in the mixing parameter-space are illustrated in Figure 7.

Finally, during the late nonlinear phase, the KH vortex becomes more and more rolled-up (right panels) leading to increasingly twisted magnetic field lines, which, in some cases, can also disrupt and generate small loops inside the vortex. The structure becomes highly distorted and displays several boundaries in correspondence with the leading edge. The resulting trajectory in the mixing parameter-space is a complex loop with twists and it is characterized by changes in direction owing to the highly distorted field lines (see the bottom right panel). It is worth noticing that if MMS would cross Type II and Type III structures through the edge and not through the center of the structure, the path in the mixing parameter-space would be similar to a linear crossing (Type I) but would not approach the bottom left part of the mixing parameter-space (where the ion and electron thresholds are) and would stop halfway. We indeed observed such partial crossings, but we discarded them from our statistical analysis presented below.

4.2. Statistics of the Crossings

Now we analyze statistically all the crossings observed during the roughly 1.5 hr of KH fluctuations. Some crossings displayed partial trajectories in the mixing parameter-space or had an ambiguous shape that could not be clearly categorized in any of the groups discussed above. We disregarded from our analysis ∼20% of data, corresponding to these types of crossings. Thus, we ended up with 69 well-defined crossings, which correspond to one of the shapes discussed in Section 4, namely, straight line, simple loop, and complex loop.

We divided the KH event into seven intervals of 20 min each and evaluated the number of each shape in that bin. To enhance counting statistics without affecting the global behavior, each bin overlaps 10 min with the previous one. The shapes whose starting and ending times belong to different bins have been counted only in the bin of the initial time, in order to avoid double counting. Finally, we evaluated the percentage of each kind of shape with respect to the total number of shapes identified in the corresponding bin. The results of the statistics are shown in Figure 8, where the *x* axis represents the central time of the corresponding 20-min interval.

The Type II group (red region) is observed during the whole KH interval with a percentage ranging between 40% at 10:39:00 UTC and 80% at 10:49:00 UTC. The Type I (blue region), instead, is mostly observed during the first part of the KH interval. The observation of Type I shapes increases until 10:29:00 UTC when the highest percentage (about 40%) is observed and then decreases until 11:09:00 UTC when there are no Type I shapes

observed. Finally, a few percentages of Type III shapes (yellow region) is observed during the first part of the KH interval, while an increasing number of these shapes is observed during the second part of the KH interval with a maximum of about 50% after 11:09:00 UTC.

According to our interpretation, each color corresponds also to a different structure. Thus, at the very beginning of the studied interval, an increasing number of linear waves is observed. However, after approximately an hour, MMS detected more and more steep waves and rolled-up vortices. Thus, a fast transition from linear to nonlinear structures is observed. This suggests that the system becomes more unstable favoring an enhancement of the KH instability over the last 30 min of the event.

5. Discussion

We have analyzed a KH event observed by MMS at the dusk flank of the Earth's magnetopause by means of both ions and electrons mixing parameters (see Equations 2 and 3). Such parameters are based on the energies of the different particles in the shear layer, where the instability takes place. The choice of the energy ranges in the definition of the mixing parameter can generally be different from event to event. As long as the energies of the MSH and MSP populations do not overlap, as is the case for the analyzed interval, we can use fixed ranges with a very good outcome. If the energies overlap, instead, the mixing parameters would not work well.

The near-Earth's environment is suitable for this method since it is characterized by the interaction of plasmas with very different properties. The low density, almost zero bulk speed, and high temperature plasma in the MSP interact with the shocked solar wind plasma of the MSH, which has high density, low temperature, and high velocity. On the contrary, the pristine solar wind, for instance, would not be suitable for this kind of approach because of the similar stream of plasma at the possible KH sites. Besides these well-distinguished properties, a good resolution for the particle instrument is also necessary in order to obtain detailed trajectories in the mixing parameter-space.

Our analysis and interpretation of the observed trajectories in the mixing parameter-space, has underlined an evolution of the KH instability from a linear to a nonlinear phase. Such transition from linear waves to rolled-up vortices is quite fast since it occurs in a short time period (~1 hr). During this interval, MMS moves from [5.19 7.19 0.23] R_E to [4.73 9.64 0.03] R_E further away from the nose of the magnetopause by approximately 3 R_E. Other *in situ* observations have shown that KH waves evolve as they propagate toward the tail and rolled-up vortices are most frequently found in the post-noon side (Lin et al., 2014; Taylor et al., 2012). However, in the present event, the distance traveled by the satellite is not sufficiently large to fully explain the observed evolution from linear waves to rolled-up vortices. Thus, what is the mechanism that leads to a rapid enhancement of the instability during this event?

The observed evolution of the KH waves can be attributed to the solar wind conditions, which change during the MMS observation. From top to bottom, Figure 9 shows the components of the magnetic field and bulk velocity observed by three different satellites embedded in the solar wind (see color legend). On the one hand, WIND and ACE were located in the same side (flank) of, or close enough to, the MMS position but hundreds of R_E upstream from the Earth; on the other hand, THEMIS B is on the opposite side but much close to the Earth's environment. For better visualization of the solar wind properties in Figure 9, we show the solar wind conditions in a temporal window larger than the KH event (yellow shade). All the quantities have been shifted to the MMS location for a direct comparison, taking into account the time delay between the spacecraft.

We observe that the bulk solar wind flow remains quite steady and mainly directed along $-x$ in GSE coordinates, and the magnetic field is varying and all the components have similar values ranging between [−20, 20] nT. While both B_x and B_z stay positive along the whole interval (panels a and b), B_y rotates during the KH interval we analyzed, switching from negative to positive values. Thus, the solar wind magnetic field is changing between two different orientations, known as Parker spiral (PS, B_x and B_y have opposite signs) and ortho-Parker spiral (OPS, B_x and B_y have the same sign). Nykyri (2013) found an opposite response of the MSH on the PS and OPS orientations, depending on the magnetopause side under consideration. The PS (OPS) leads to a quasi-perpendicular shock on the dusk (dawn) side (Tsurutani & Rodriguez, 1981). According to the Rankine-Hugoniot jump conditions, the tangential component of the magnetic field is enhanced at the quasi-perpendicular side, producing high magnetic compression. On the contrary, at the quasi-parallel shock (which in the PS configuration is at the

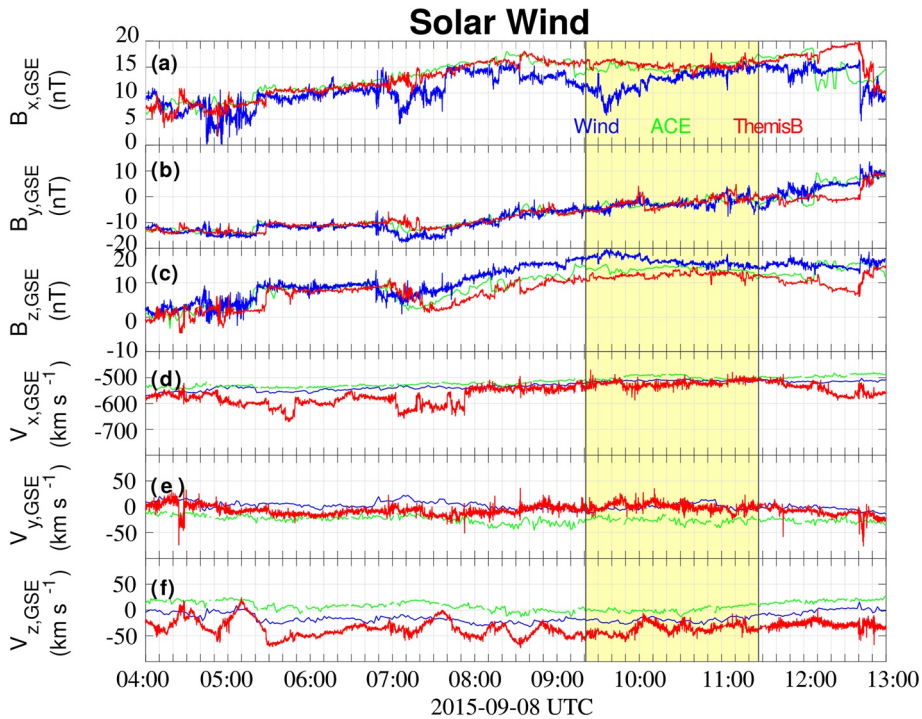

Figure 9. Solar wind observations by the three satellites WIND, ACE, and THEMIS B during the time interval from 04:00 to 13:00 UTC. The measurements have been time shifted to the magnetospheric multiscale (MMS) location in order to make a point-to-point comparison. All the quantities are in the Geocentric Solar Ecliptic coordinate system. From top to bottom: (a) x component of the magnetic field; (b) y component of the magnetic field; (c) z component of the magnetic field; (d) x component of the solar wind speed; (e) y component of the solar wind speed; (f) z component of the solar wind speed. The yellow shade indicates the time of the Kelvin-Helmholtz observation by MMS.

dawnside) the magnetic field lines are less compressed due to the lower amplitude of the tangential magnetic field. The solar wind in the present event is switching from a PS to an OPS; thus, at the duskside, the magnetic field, which was at first highly compressed, then becomes less compressed.

The effect of the solar wind conditions on the MSH plasma is twofold. On the one hand, the steady bulk flow does not affect the plasma compression at the magnetopause and leaves unchanged the velocity jump across the shear layer; on the other hand, the change of the magnetic field orientation decreases the tangential component of the magnetic field at the dusk side enhancing the growth rate of the KH instability. Indeed, Equation 1, shows that the magnetic field along the shear layer has a stabilizing effect on the instability. Then, the switch from the PS to the OPS leads to a smaller tangential component in the dusk than the dawn side and consequently an enhancement of the KH growth rate, which explains the increasing number of rolled-up vortices during the last part of the event.

6. Conclusions

We have analyzed MMS observation of a Kelvin-Helmholtz event by means of the mixing parameter, which measures the mixing degree between plasmas with well distinct properties. This condition is well satisfied in the near Earth's environment, where the MSP and MSH plasmas have clearly different energies. In spacecraft measurements, we do not have control of where are the particles coming from, but we can use such a quantity to identify the origin of particles based on differences in their energy. In addition, the mixing parameter displays boundaries in correspondence of sharp gradients in the magnetic field, current sheets, and transition regions in the energy spectrogram, thus it can likely identify Kelvin-Helmholtz vortices and boundaries when the particle energies are well distinguished.

We conducted our analysis of the Kelvin-Helmholtz event in the parameter-space generated by the ion and electron mixing. We found that the mixing parameter follows different trajectories, which correspond to a certain KH

structure. Indeed, we distinguished three typical shapes: a straight line, a simple loop, and a complex loop which correspond to the crossing of a linear wave, steepened wave, and rolled-up vortex, respectively.

A more statistical analysis of these results showed that the mixing parameter becomes more and more complicated as the instability is enhanced. We observed that the majority of the 69 well-defined shapes we observed is a simple loop, but linear waves and rolled-up vortices are also observed at the very beginning and at the end of the interval, respectively. The transition that we observe is consistent with changes in the solar wind conditions. Indeed, the tangential component of the magnetic field is decreasing in the last part of the event, leading to an enhancement of the Kelvin-Helmholtz instability and to the development of more and more rolled-up vortices.

Data Availability Statement

The data used in this paper are freely available from the MMS data center (https://lasp.colorado.edu/mms/sdc/public/about/browse-wrapper/).

Acknowledgments
This work has received funding from the European Unions Horizon 2020 research and innovation programme under grant agreement no. 776262 (AIDA, www.aida-space.eu). YVK and DBG acknowledge support from the Swedish Research Council, Grant 2016-05,507, and Swedish National Space Agency (SNSA) Grant 128/17. We thank Dr Emiliya Yordanova for the helpful discussion. Open Access Funding provided by Universita della Calabria within the CRUI-CARE Agreement.

References

Axford, W. I., & Hines, C. O. (1961). A unifying theory of high-latitude geophysical phenomena and geomagnetic storms. *Canadian Journal of Physics*, *39*, 1433–1464. https://doi.org/10.1139/p61-172

Chandrasekhar, S. (1961). *Hydrodynamic and hydromagnetic stability*. Dover Publications. https://ui.adsabs.harvard.edu/abs/1961hhs..book.....C

Chen, L., & Hasegawa, A. (1974). A theory of long-period magnetic pulsations: 1. Steady state excitation of field line resonance. *Journal of Geophysical Research*, *79*(7), 1024–1032. https://doi.org/10.1029/JA079i007p01024

Daughton, W., Nakamura, T. K. M., Karimabadi, H., Roytershteyn, V., & Loring, B. (2014). Computing the reconnection rate in turbulent kinetic layers by using electron mixing to identify topology. *Physics of Plasmas*, *21*(5), 052307. https://doi.org/10.1063/1.4875730

Dimmock, A. P., Osmane, A., Pulkkinen, T. I., & Nykyri, K. (2015). A statistical study of the dawn-dusk asymmetry of ion temperature anisotropy and mirror mode occurrence in the terrestrial dayside magnetosheath using THEMIS data. *Journal of Geophysical Research*, *120*(7), 5489–5503. https://doi.org/10.1002/2015ja021192

Drazin, P. G. (2002). *Introduction to hydrodynamic stability*. Cambrudge Univesity Press. https://ui.adsabs.harvard.edu/abs/2002ihs..book.....D

Eriksson, S., Lavraud, B., Wilder, F. D., Stawarz, J. E., Giles, B. L., Burch, J. L., et al. (2016). Magnetospheric Multiscale observations of magnetic reconnection associated with Kelvin-Helmholtz waves. *Journal of Geophysical Research*, *43*(11), 5606–5615. https://doi.org/10.1002/2016GL068783

Faganello, M., & Califano, F. (2017). Magnetized Kelvin-Helmholtz instability: Theory and simulations in the Earth's magnetosphere context. *Journal of Plasma Physics*, *83*(6), 535830601. https://doi.org/10.1017/S0022377817000770

Faganello, M., Califano, F., & Pegoraro, F. (2008). Competing mechanisms of plasma transport in inhomogeneous configurations with velocity shear: The solar-wind interaction with Earth's magnetosphere. *Physical Review Letter*, *100*(1), 015001. https://doi.org/10.1103/PhysRevLett.100.015001

Fairfield, D. H., Otto, A., Mukai, T., Kokubun, S., Lepping, R. P., Steinberg, J. T., & Yamamoto, T. (2000). Geotail observations of the Kelvin-Helmholtz instability at the equatorial magnetotail boundary for parallel northward fields. *Journal of Geophysical Research*, *105*(A9), 21159–21173. https://doi.org/10.1029/1999ja000316

Foullon, C., Farrugia, C. J., Fazakerley, A. N., Owen, C. J., Gratton, F. T., & Torbert, R. B. (2008). Evolution of Kelvin-Helmholtz activity on the dusk flank magnetopause. *Journal of Geophysical Research*, *113*(A11), A11203. https://doi.org/10.1029/2008JA013175

Foullon, C., Verwichte, E., Nakariakov, V. M., Nykyri, K., & Farrugia, C. J. (2011). Magnetic Kelvin-Helmholtz instability at the Sun. *The Astrophysical Journal Letter*, *729*(1), L8. https://doi.org/10.1088/2041-8205/729/1/l8

Hasegawa, H., Fujimoto, M., Phan, T. D., Rème, H., Balogh, A., Dunlop, M. W., et al. (2004). Transport of solar wind into Earth's magnetosphere through rolled-up Kelvin-Helmholtz vortices. *Nature*, *430*(7001), 755–758. https://doi.org/10.1038/nature02799

Hasegawa, H., Fujimoto, M., Takagi, K., Saito, Y., Mukai, T., & RèMe, H. (2006). Single-spacecraft detection of rolled-up Kelvin-Helmholtz vortices at the flank magnetopause. *Journal of Geophysical Research*, *111*(A9), A09203. https://doi.org/10.1029/2006JA011728

Henri, P., Califano, F., Faganello, M., & Pegoraro, F. (2012). Magnetised Kelvin-Helmholtz instability in the intermediate regime between subsonic and supersonic regimes. *Physics of Plasmas*, *19*(7), 072908. https://doi.org/10.1063/1.4739234

Henri, P., Cerri, S. S., Califano, F., Pegoraro, F., Rossi, C., Faganello, M., et al. (2013). Nonlinear evolution of the magnetized Kelvin-Helmholtz instability: From fluid to kinetic modeling. *Physics of Plasmas*, *20*(10), 102118. https://doi.org/10.1063/1.4826214

Henry, Z. W., Nykyri, K., Moore, T. W., Dimmock, A. P., & Ma, X. (2017). On the dawn-dusk asymmetry of the Kelvin-Helmholtz instability between 2007 and 2013. *Journal of Geophysical Research*, *122*(12), 11888. https://doi.org/10.1002/2017JA024548

Kavosi, S., & Raeder, J. (2015). Ubiquity of Kelvin-Helmholtz waves at Earth's magnetopause. *Nature Communications*, *6*, 7019. https://doi.org/10.1038/ncomms8019

Kieokaew, R., Lavraud, B., Yang, Y., Matthaeus, W. H., Ruffolo, D., Stawarz, J. E., & Angelini, V. (2021). Solar orbiter observations of the Kelvin-Helmholtz instability in the solar wind. *Astronomy and Astrophysics*, *656*, A12. https://doi.org/10.1051/0004-6361/202140915

Kivelson, M. G., & Chen, S.-H. (1995). *The magnetopause: surface waves and instabilities and their possible dynamical consequences*. Washington DC American Geophysical Union Geophysical Monograph Series, 90, 257–268. https://doi.org/10.1029/GM090p0257

Lakhina, G. S., & Tsurutani, B. T. (1999). A generation mechanism for the polar cap boundary layer broadband plasma waves. *Journal of Geophysical Research*, *104*(A1), 279–291. https://doi.org/10.1029/98JA02724

Li, W., André, M., Khotyaintsev, Y. V., Vaivads, A., Graham, D. B., Toledo-Redondo, S., et al. (2016). Kinetic evidence of magnetic reconnection due to Kelvin-Helmholtz waves. *Journal of Geophysical Research*, *43*(11), 5635–5643. https://doi.org/10.1002/2016GL069192

Li, W. Y., Guo, X. C., & Wang, C. (2012). Spatial distribution of Kelvin-Helmholtz instability at low-latitude boundary layer under different solar wind speed conditions. *Journal of Geophysical Research*, *117*(A8), A08230. https://doi.org/10.1029/2012JA017780

Lin, D., Wang, C., Li, W., Tang, B., Guo, X., & Peng, Z. (2014). Properties of Kelvin-Helmholtz waves at the magnetopause under northward interplanetary magnetic field: Statistical study. *Journal of Geophysical Research*, *119*(9), 7485–7494. https://doi.org/10.1002/2014JA020379

Ma, X., Otto, A., & Delamere, P. A. (2014a). Interaction of magnetic reconnection and Kelvin-Helmholtz modes for large magnetic shear: 1. Kelvin-helmholtz trigger. *Journal of Geophysical Research*, *119*(2), 781–797. https://doi.org/10.1002/2013JA019224

Ma, X., Otto, A., & Delamere, P. A. (2014b). Interaction of magnetic reconnection and Kelvin-Helmholtz modes for large magnetic shear: 2. Reconnection trigger. *Journal of Geophysical Research*, *119*(2), 808–820. https://doi.org/10.1002/2013JA019225

Matsumoto, Y., & Hoshino, M. (2004). Onset of turbulence induced by a Kelvin-Helmholtz vortex. *Journal of Geophysical Research*, *31*(2), L02807. https://doi.org/10.1029/2003GL018195

Miura, A. (1982). Nonlinear evolution of the magnetohydrodynamic Kelvin-Helmholtz instability. *Physical Review Letter*, *49*(11), 779–782. https://doi.org/10.1103/PhysRevLett.49.779

Nakamura, T. K. M., & Daughton, W. (2014). Turbulent plasma transport across the Earth's low-latitude boundary layer. *Journal of Geophysical Research*, *41*(24), 8704–8712. https://doi.org/10.1002/2014GL061952

Nakamura, T. K. M., Hasegawa, H., Daughton, W., Eriksson, S., Li, W. Y., & Nakamura, R. (2017). Turbulent mass transfer caused by vortex induced reconnection in collisionless magnetospheric plasmas. *Nature Communications*, *8*, 1582. https://doi.org/10.1038/s41467-017-01579-0

Nykyri, K. (2013). Impact of MHD shock physics on magnetosheath asymmetry and Kelvin-Helmholtz instability. *Journal of Geophysical Research*, *118*(8), 5068–5081. https://doi.org/10.1002/jgra.50499

Nykyri, K., & Dimmock, A. P. (2016). Statistical study of the ULF Pc4-Pc5 range fluctuations in the vicinity of Earth's magnetopause and correlation with the Low Latitude Boundary Layer thickness. *Advances in Space Research*, *58*(2), 257–267. https://doi.org/10.1016/j.asr.2015.12.046

Nykyri, K., & Otto, A. (2001). Plasma transport at the magnetospheric boundary due to reconnection in Kelvin-Helmholtz vortices. *Journal of Geophysical Research*, *28*(18), 3565–3568. https://doi.org/10.1029/2001GL013239

Nykyri, K., Otto, A., Lavraud, B., Mouikis, C., Kistler, L. M., Balogh, A., & Rème, H. (2006). Cluster observations of reconnection due to the Kelvin-Helmholtz instability at the dawnside magnetospheric flank. *Annales Geophysicae*, *24*(10), 2619–2643. https://doi.org/10.5194/angeo-24-2619-2006

Otto, A., & Fairfield, D. H. (2000). Kelvin-Helmholtz instability at the magnetotail boundary: MHD simulation and comparison with Geotail observations. *Journal of Geophysical Research*, *105*(A9), 21175–21190. https://doi.org/10.1029/1999JA000312

Plaschke, F., Kahr, N., Fischer, D., Nakamura, R., Baumjohann, W., Magnes, W., et al. (2016). Steepening of waves at the duskside magnetopause. *Journal of Geophysical Research*, *43*(14), 7373–7380. https://doi.org/10.1002/2016GL070003

Plaschke, F., Taylor, M. G. G. T., & Nakamura, R. (2014). Alternative interpretation of results from Kelvin-Helmholtz vortex identification criteria. *Journal of Geophysical Research*, *41*(2), 244–250. https://doi.org/10.1002/2013GL058948

Pollock, C., Moore, T., Jacques, A., Burch, J., Gliese, U., Saito, Y., et al. (2016). Fast plasma investigation for magnetospheric Multiscale. *Social Science Research*, *199*(1–4), 331–406. https://doi.org/10.1007/s11214-016-0245-4

Russell, C. T., Anderson, B. J., Baumjohann, W., Bromund, K. R., Dearborn, D., Fischer, D., et al. (2016). The magnetospheric multiscale magnetometers. *Social Science Research*, *199*(1–4), 189–256. https://doi.org/10.1007/s11214-014-0057-3

Settino, A., Malara, F., Pezzi, O., Onofri, M., Perrone, D., & Valentini, F. (2020). Kelvin-Helmholtz instability at proton scales with an exact kinetic equilibrium. *The Astrophysical Journal*, *901*(1), 17. https://doi.org/10.3847/1538-4357/abada9

Settino, A., Perrone, D., Khotyaintsev, Y. V., Graham, D. B., & Valentini, F. (2021). Kinetic features for the identification of Kelvin-Helmholtz vortices in in situ observations. *The Astrophysical Journal*, *912*(2), 154. https://doi.org/10.3847/1538-4357/abf1f5

Sorriso-Valvo, L., Catapano, F., Retinò, A. r., Le Contel, O., Perrone, D., Roberts, O. W., et al. (2019). Turbulence-driven ion beams in the magnetospheric Kelvin-Helmholtz instability. *Physical Review Letter*, *122*(3), 035102. https://doi.org/10.1103/PhysRevLett.122.035102

Stawarz, J. E., Eriksson, S., Wilder, F. D., Ergun, R. E., Schwartz, S. J., Pouquet, A., et al. (2016). Observations of turbulence in a Kelvin-Helmholtz event on 8 September 2015 by the magnetospheric multiscale mission. *Journal of Geophysical Research*, *121*(11), 11021. https://doi.org/10.1002/2016JA023458

Takagi, K., Hashimoto, C., Hasegawa, H., Fujimoto, M., & Tandokoro, R. (2006). Kelvin-Helmholtz instability in a magnetotail flank-like geometry: Three-dimensional MHD simulations. *Journal of Geophysical Research*, *111*(A8), A08202. https://doi.org/10.1029/2006JA011631

Taylor, M. G. G. T., Hasegawa, H., Lavraud, B., Phan, T., Escoubet, C. P., Dunlop, M. W., et al. (2012). Spatial distribution of rolled up Kelvin-Helmholtz vortices at Earth's dayside and flank magnetopause. *Annales Geophysicae*, *30*(6), 1025–1035. https://doi.org/10.5194/angeo-30-1025-2012

Tsurutani, B. T., Arballo, J. K., Galvan, C., Zhang, L. D., Zhou, X.-Y., Lakhina, G. S., et al. (2001). Polar cap boundary layer waves: An auroral zone phenomenon. *Journal of Geophysical Research*, *106*(A9), 19035–19055. https://doi.org/10.1029/2000JA003007

Tsurutani, B. T., Lakhina, G. S., Ho, C. M., Arballo, J. K., Galvan, C., Boonsiriseth, A., et al. (1998). Broadband plasma waves observed in the polar cap boundary layer: Polar. *Journal of Geophysical Research*, *103*(A8), 17351–17366. https://doi.org/10.1029/97JA03063

Tsurutani, B. T., & Rodriguez, P. (1981). Upstream waves and particles—An overview of ISEE results. *Journal of Geophysical Research*, *86*(A6), 4317–4324. https://doi.org/10.1029/JA086iA06p04317

Tsurutani, B. T., & Thorne, R. M. (1982). Diffusion processes in the magnetopause boundary layer. *Geophysical Research Letter*, *9*(11), 1247–1250. https://doi.org/10.1029/GL009i011p01247

Vernisse, Y., Lavraud, B., Eriksson, S., Gershman, D. J., Dorelli, J., Pollock, C., et al. (2016). Signatures of complex magnetic topologies from multiple reconnection sites induced by Kelvin-Helmholtz instability. *Journal of Geophysical Research*, *121*(10), 9926–9939. https://doi.org/10.1002/2016JA023051